

Laboratory investigation of the interaction between the jet and background, from collisionless to strong collision

Z. Lei,¹ Z. H. Zhao,¹ Y. Xie,¹ W. Q. Yuan,¹ L. X. Li,¹ H. C. Gu,² X. Y. Li,³ B.Q. Zhu,⁴ J.Q. Zhu,⁴ S.P. Zhu,⁵ X.T. He,⁵ and B. Qiao*¹

¹*Center for Applied Physics and Technology, HEDPS, and State Key Laboratory of Nuclear Physics and Technology, School of Physics, Peking University, Beijing 100871, P. R. China;*

²*Beijing National Laboratory for Condensed Matter Physics, Institute of Physics, Chinese Academy of Sciences, Beijing 100190 P. R. China*

³*Department of Plasma Physics and Fusion Engineering, CAS Key Laboratory of Geospace Environment, University of Science and Technology of China, Hefei, Anhui 230026, People's Republic of China*

⁴*National Laboratory on High Power Laser and Physics, Chinese Academy of Sciences, Shanghai 201800, People's Republic of China;*

⁵*Institute of Applied Physics and Computational Mathematics, Beijing 100094, P. R. China*

(Dated: 15 March 2022)

The interaction between the supersonic jet and background can influence the process of star formation, and this interaction also results in a change of the jet's velocity, direction and density through shock waves. However, due to the limitations of current astronomical facilities, the fine shock structure and the detailed interaction process still remain unclear. Here we investigate the plasma dynamics under different collision states through laser-driven experiments. A double-shock structure is shown in the optical diagnosis for collision case, but the integrated self-emitting X-ray characteristic is different. For solid plastic hemisphere obstacle, two-layer shock emission is observed, and for the relatively low density laser-driven plasma core, only one shock emission is shown. And the plasma jets are deflected by 50° through the interaction with the high-density background in both cases. For collisionless case, filament structures are observed, and the mean width of filaments is roughly the same as the ion skin depth. High-energy electrons are observed in all interaction cases. We present the detail process of the shock formation and filament instability through 2D/3D hydrodynamic simulations and particle-in-cell simulations respectively. Our results can also be applied to explain the shock structure in the Herbig-Haro (HH) 110/270 system, and the experiments indicate that the impact point may be pushed into the inside part of the cloud.

The interaction between the supersonic collimated jets and the background has long been a topic of great astrophysical interest^{1,2}. The collision of the jet and the interstellar or intergalactic media (ISM, IGM) can trigger the shock structures within the background. And these shocks will compress and heat the clouds. If the initial cloud is dense enough, the positive feedback of these shocks will induce the star formation^{3,4}. Many observations^{5,6} and numerical simulation results^{4,7,8} have shown the positive effect on the jet-induced star formation. High energy cosmic rays are also believed to be related with this interaction^{9,10}. Collisionless shocks are formed when ultrahigh speed plasma jets interacts with the backgrounds, and the magnetic field is generated by Weibel instability. The kinetic energy of plasma jets is dissipated via wave-particle collective interaction. The collisionless shock can accelerate charged particles to extremely high energies through Fermi acceleration mechanism¹¹.

The interaction also results in the change of the jet's direction, velocity, density, etc. HH jets are collimated plasma flows, which are commonly driven by the young stellar objects. However, for the HH 110 jet, astronomers failed to find the corresponding driven source through careful searches at optical, infrared and sub-mm wavelengths¹². And some observational evidences show that the driving source of HH 110 jet is HH 270 jet^{12,14}. The HH 270 jet interacts with a high-density molecular cloud core through strong collision. The collision shock deflects the jet then HH 110 jet appears, and the opening angle of HH 110 is large ($\sim 10^\circ$). It also has more chaotic structure, which is reminiscent of a turbulent flow¹⁵. According to theoretical analysis and numerical simulations¹⁶⁻¹⁸, a double-layer shock structure should be formed during the interaction between the jet and cloud. The first shock can deflect the incident jet to a new direction. The second shock travels into the background, then compresses and heats the background cloud. However, some observation results¹³ show that there is only the shocked deflection jet, and no shock emission is detected in the impact region in which the axis of HH 270 crosses the axis of HH 110, so they¹³ disagreement with a jet-cloud collision model. Though the observations mentioned above provide elaborate information about the deflected jet, the fine shock structure and the detailed interaction process still remain unclear.

Developing the high-power pulse facilities can help significantly in addressing this interaction process. Laboratory experiments has become a new method for studying the astrophysical phenomena and verifying theoretical models¹⁹⁻²¹. Although there are huge differences in scales, the laboratory plasma can be scaled up to the astrophysical objects

through the scaling laws of magneto-hydrodynamics^{22,23}. And the process of jet deflection has been investigated by laboratory experiments. Lebedev et al. studied the jet deflection via crosswinds by using the MAGPIE pulsed power machine²⁴, and the deflection angle is dependent on the ram pressure ($p = \rho v^2$) of the crosswind. Shocks within the jet beam seem to appear in the image data. Yuan et al. presented the laser-driven plasma jet was deflected by the ram pressure of cross-wind²⁵. Hartigan et al.²⁶ showed the results of laser-driven supersonic plasma jet is deflected by a spherical obstacle. The obstacle was destroyed by the plasma jet, and some filament structures appeared. However, all the experiments mentioned above do not concern the emission structure of the deflection process, and the collision state are fully strong collision.

In this paper, we present the whole process of the interaction between the copper (Cu) plasma jet and the plastic (CH) background, from collisionless to strong collision. There are two forms of background plasma. The first one is generated from the laser-ablating plane CH target, and the second is CH hemisphere obstacle. More details of target configuration are shown in experiment setup. The supersonic plasma jet is generated by the V-shape Cu target. For collisionless situation, the filament structures appear due to the Weibel instability, and the mean width of filaments is roughly in consistent with the ion skin depth. The PIC simulations also reproduce the experiment results. For strong collisional situation, the plasma jet is deflected by the high-density laser-driven CH plasma core, and a bow-shape like working surface is also observed at the front of the deflected jet. The deflection angle is about 50° . A double-shock structure is clearly shown in the optical images. And a two-layer shock emission characteristic is also shown in self-emitting X-ray data when the plasma jet directly interacts with the CH hemisphere obstacle, but it is different with the former case. Kelvin-Helmholtz (KH) instability grows in the interaction surface, and the self-generated magnetic field is amplified. These findings are verified by radiation magneto-hydrodynamic (RMHD) simulations. And the electrons are observed to be accelerated up to higher energy in the interaction cases than the jet-only case. When the localization criteria and the scaling laws are met, the experiments can be applied to the HH 110/270 system. We infer the chaotic structure of HH 110 jet is because of the KH instability, and the impact point for the HH 270 jet and the dense cloud is pushed to the inside due to the forward shock.

I. RESULTS

Experimental setup. Our experiments are carried out at ShenGuang-II (SG-II) laser facility in Shanghai, China. Three different types of targets are applied in our experiments, and the main difference is the structure of the CH target (plane or hemisphere). And Fig 1(e) to (g) show details of the three types of target. As shown in 1(a), for the CH plain targets, the background plasma is generated by the interaction between the laser and hydrocarbon target, and a semi-spherical like plasma outflow appear in the front of the target. This type of target is similar to Yuan's setup²⁵, but our system size is larger. Then the background plasma is full of interaction region, and not like the crosswind structure. For the CH hemisphere target, the plasma jet can directly interact with this high density background. The V-shaped targets were constructed with two $500 \mu\text{m}$ thick and $1 \text{ mm} \times 1 \text{ mm}$ Cu foils, which have opening angle of 120° . Each foil is driven by two laser beams, and a plasma plume can be generated on each foil. The Cu plasma jet is formed by the convergence of two plasma plumes²⁷. And more details of the driven lasers are given in Methods section.

A probe laser is used to diagnose the plasma evolution, which is transversely passing through the interaction region. Shadowgraphy and interferometry are both applied in our experiments, whose details are shown in Supplementary Fig. S1. And our experiments were divided into two rounds with different probe beams. In the first round, the ninth beam of SG-II laser facility was used to be the probe laser, with a wavelength of 527 nm, duration of 30 ps, and energy of 15 J. While in the second round, the probe pulse duration was 6.5 ns with 15 mJ energy. To match the diagnostic condition, the probe laser was cut into a 120 ps pulse with a gated optical image (GOI). In the following optical images, the gray images are obtained in the first round, and the green images are in the second round. The time delay between the probe laser and the driven laser is labeled as T_{probe} , as shown in Fig 1(b). The number density can be obtained through the Nomarski interferometer image. As shown in figure 1(c) and (d), the number density of Cu plasma jet are respectively given at 3 ns and 4 ns ($T_{probe} = T_0 + 3 \text{ or } 4 \text{ ns}$). According to the length of jet in different probe time, the velocity of the Cu plasma jet is about 800 km/s, and the mean number density is about $2 \times 10^{19} \text{ cm}^{-3}$. The self-emitting X-rays of plasma are detected by the pinhole camera, and the observation angle is 45° to the horizontal plane. The electron energy spectrum can be recorded by the electron spectrometer.

Free expansion of laser-driven CH background and Cu jet. Figure 2(a) show the CH background plasma evolution at 3 ns, and the corresponding number density of the light blue area in panel (a) is given in 2(b). The CH plasma outflow is close to isotropic expansion, and the number density gradually decreases from center to radially outward. Within $500 \mu\text{m}$ from the focal spot, the number density is about higher than $1 \times 10^{20} \text{ cm}^{-3}$. The lateral expansion velocity of the CH plasma outflow can be estimated about 400km/s.

A three-dimensional radiation hydrodynamic simulation is also implemented to reproduce the experiment results,

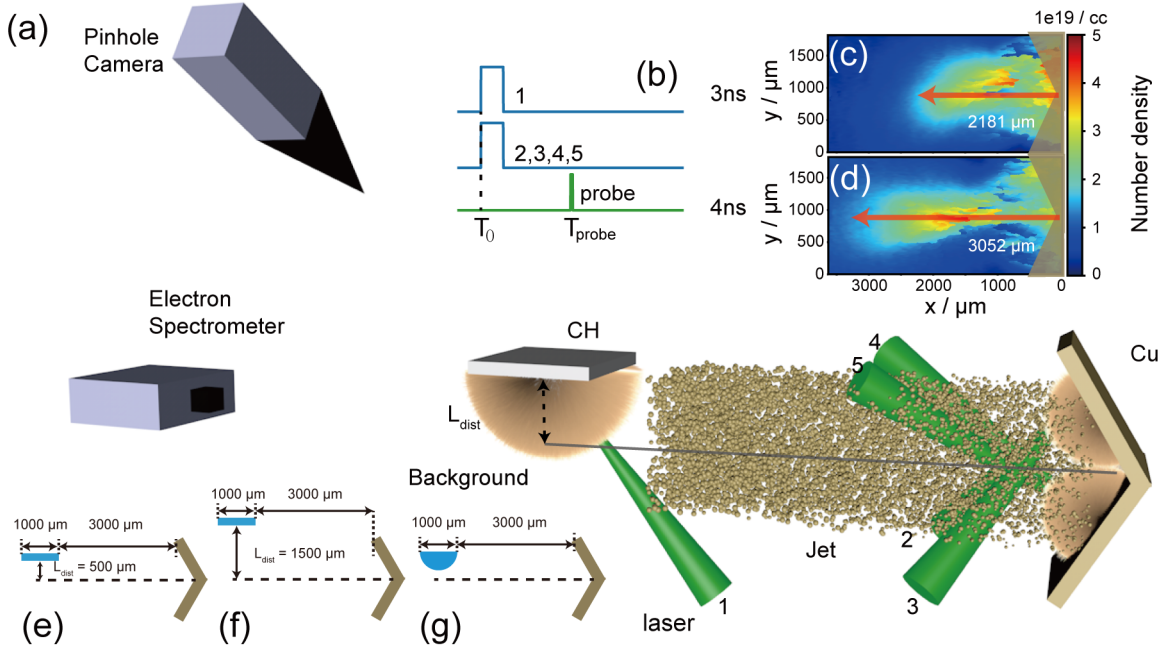


FIG. 1. **Schematic view of the experimental setup.** As shown in panel (a), the background plasma is generated by the interaction between the laser and hydrocarbon (CH) target (grey), and the collimation jet is driven by nanosecond (ns) laser pulses ('2' - '5') from the K-shape copper (Cu) target (golden). The L_{dist} represents the distance between the CH target and the axis of Cu target is $3000 \mu\text{m}$, which can be considered as the system size. The electron spectrometer is placed in the front of the Cu target. The X-ray radiation of plasma is detected by the pinhole camera. The evolution of plasma is diagnosed by the shadowgraphy and interferometry method with a short probe beam (perpendicular to the paper). And the time delays of different laser pulses as well that of the probe laser for the optical Nomarski interferometer diagnostics are given in panel (b). Panel (c) and (d) show the maps of the inferred electron number density through phase difference, in $[\text{cm}^{-3}]$ at 3 ns and 4 ns respectively. Panel (e) to (g) are the three target configurations used in the experiment

and the simulation parameters are given in Methods section. As shown in Fig 2(c), the lateral expansion of plasma outflow is slightly slower than the vertical direction (perpendicular to the target surface). And the lateral expansion velocity is about 450 km/s . The number density of the axis is given in Fig 2(d). The triangle points represent the number density of experiment in 2(b). And these results clearly show that the distribution of number density in the numerical simulation is roughly consistent with the experiment at the same location. The time-varying number density of background plasma at $500 \mu\text{m}$ and $1500 \mu\text{m}$ to the CH target is plotted in Supplementary Fig. S2. This result can also help us to identify the collision state at different time. For the Cu plasma jet, the 2D slices of electron number density and temperature are given in Fig 2(e) and (f). The morphology of the jet is similar to the experimental result, and the mean velocity is about 850 km/s . The mean temperature of Cu jet is about 300 eV , and the corresponding sound speed c_s is about 122 km/s . ($c_s = (\gamma Z k_B T / m_i)^{1/2}$, where γ is the adiabatic index; k_B is Boltzmann's constant; Z, T and m_i represent the charge state, temperature and mass number of the jet respectively). The Mach number $M_a = v/c_s$ is about 7, so that the Cu plasma jet is supersonic.

In order to show the role of Coulomb collisions in this experiment setup, we need to compare the mean free paths for collisions between the CH plasma background and the Cu plasma jet with the system size. And details of the calculation is given in Methods section. The mean free path is plotted in Fig 2(d), and the green dot line represents that the mean free path is $3000 \mu\text{m}$, which is also equivalent to the system size. When the distance between the CH target and the axis of Cu target $L_{\text{dist}} = 1500 \mu\text{m}$ (L_{dist} is labeled in 1(a)), the ion number density there is always low, so the interaction between the jet and background is fully collisionless situation. When we adjust the L_{dist} to $500 \mu\text{m}$, the ion number density at the front of CH plasma background is relative low. While at the core part, the ion number density is about $1 \times 10^{20} \text{ cm}^{-3}$, so the interaction between the jet and background would transition from collisionless to weak collision and final to strong collision. We can modify the trigger time of probe laser to observe the different collision states. When the plasma jet directly interacts with the CH hemisphere target, the collision state is fully strong collision.

The interaction between jet and background under different conditions. As the analysis above, due to

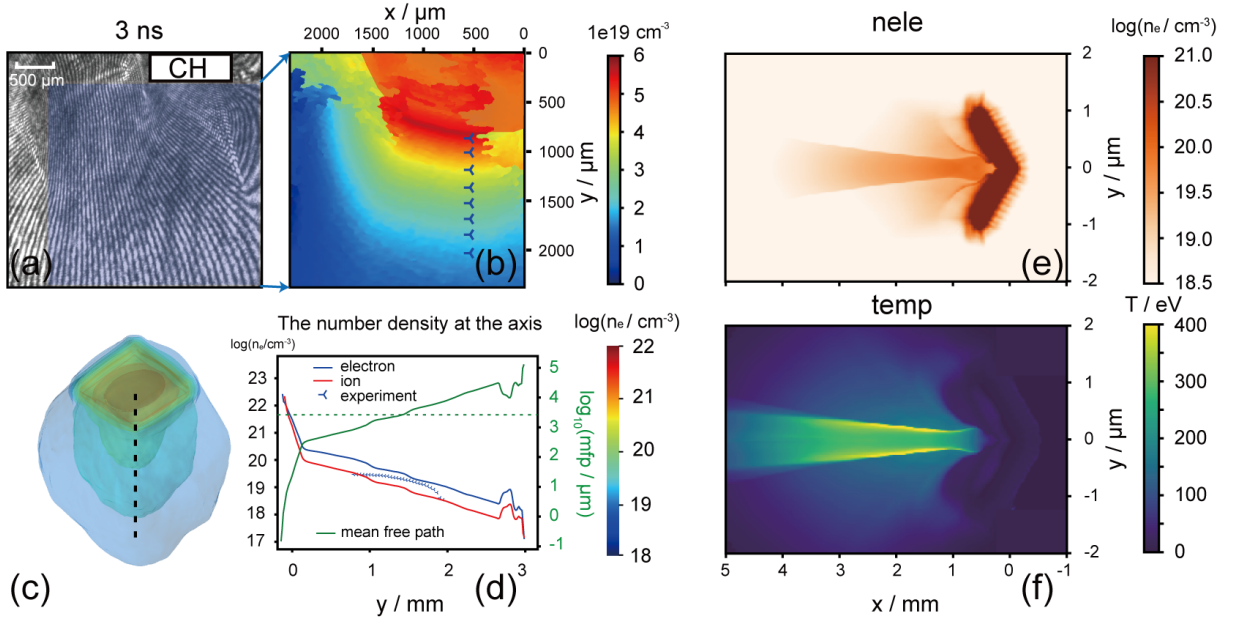


FIG. 2. **The free expansion of CH background plasma and Cu jet.** The interferometry image of CH plasma at 3 ns is given in panel (a) and the corresponding map of number density is shown in panel (b). We use the three dimensional radiation hydrodynamic simulation to reproduce the expansion process, as shown in panel (c). Panel (d) plot the number density of electrons and ions in the axis, and also the mean free path of Cu plasma jet. The triangle points represent the number density of experiment results in panel (b), and the green dot line represents the system size ($3000\mu\text{m}$.) The 2D slices of electron number density and temperature about the 3D numerical simulation of Cu plasma jet at 4 ns are shown in panel (e) and (f)

the distribution of CH plasma background, the collision state varies with the distance from the center focal point of CH target. As shown in Fig 3(a) to (c), we directly observe the dynamic evolution of the interaction between the jet and CH background. To show the jet clearly, we reverse the color of these image, so the white part is the high density region. At 3 ns, the Cu jet meets the CH background at about $1800\mu\text{m}$ from the center of CH target, and the mean free path is about $5000\mu\text{m}$, which is much larger than the interaction region. Some filament-like structures appear at the jet front, and according to the Fig 3(g), the mean full width at half maximum (FWHM) of these filaments is about $80\mu\text{m}$. As the jet continues to penetrate into the background, the number density of CH plasma increases gradually. The MFP decreases to $1000\sim 2000\mu\text{m}$, and the plasma is close to a weak collision state. When the Cu plasma jet interacts with the high-density core part, the dynamics of jet is totally different with the collisionless situation. As shown in 3(c), a strong shock (the green arrow) appears when jet contacts with the high-density part, and the MFP is about $50\sim 100\mu\text{m}$, which represents the strong collision state. Comparing with the image at 4 ns (3(b)), the high density background is a little compressed by the Cu jet. Then the jet deflects downward due to strong collision, and the deflection angle is about 50° .

In the second round, we are chiefly concerned with the latter evolution of deflected jets and the strong collision process. The shadowgraphy of the free expansion of CH background at $T_0 + 5\text{ ns}$ is shown in Fig 3(d). And the shadowgraph systems are used to indicate the variation of the second derivatives of the index of refraction, so they are often used to detect the shock wave, in which density gradient is quite big. When the plasma jet interacts with the background, the high-density core of CH plasma is compressed, and a bow-shape like working surface appears in the jet deflection direction (as shown the red arrow in Fig. 3(e)). And according to the Nomarski interferometer image (3(f)), the deflected jet still maintains collimation structure. At $T_0 + 6\text{ ns}$ (3(h)), two shock structure is formed (the black and blue arrows), and the Cu plasma jet is deflected along the first shock wave. The high-density CH background is significantly compressed, and the compression speed is estimated to 200 km/s . The impact point is pushed into the inside of CH background. The compression speed can be estimated by the pressure equilibrium, and more details are shown in the simulation results.

When we increase L_{dist} to $1500\mu\text{m}$, the collision state is the fully collisionless situation, as shown in 4(a) at 4 ns. Comparing with the 3(b), there are still distinct filament structures, and the mean FWHM is about $85\mu\text{m}$ (4(b)). According to the theoretical results²⁸, the collision can be a stabilizing term and the growth rate of Weibel instability is suppressed. Our experiment results are also consistent with the theoretical analysis. When the Cu plasma jet directly interacts with the high-density CH hemisphere target, the morphology is similar to the case of $L_{dist} = 500\mu\text{m}$.

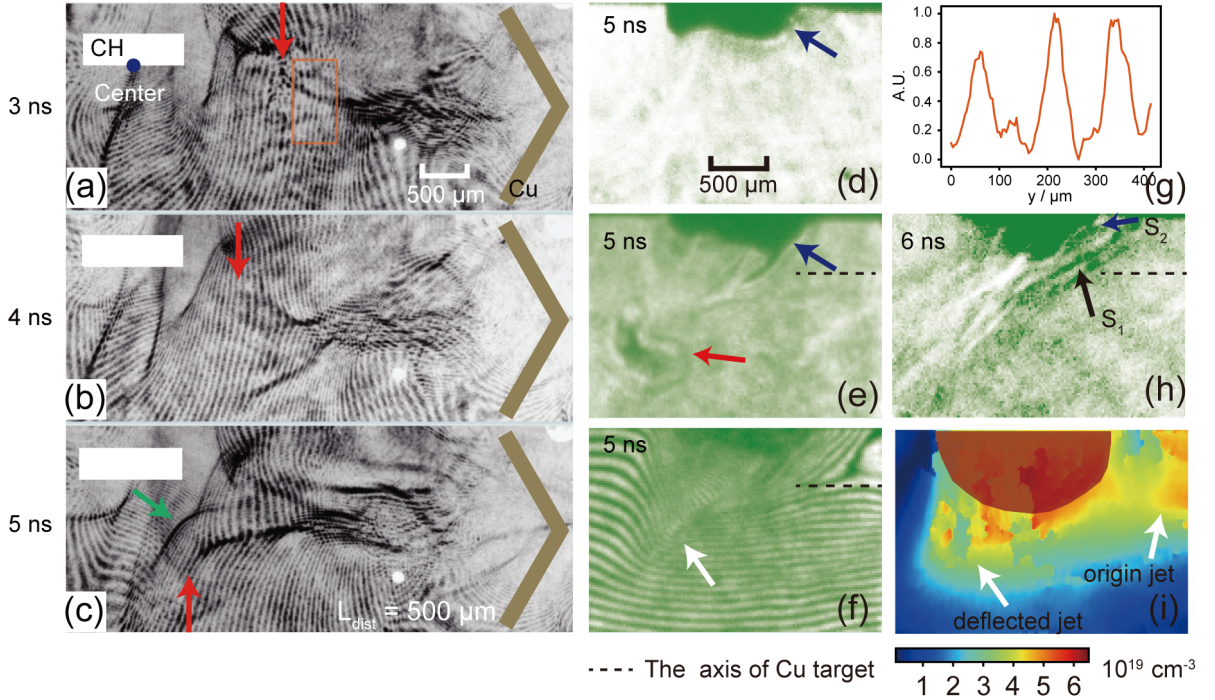


FIG. 3. **The experiment results of interaction between jet and background at $L_{\text{dist}} = 500\mu\text{m}$.** These experiment results are from two rounds. For the panel (a) to (c), they are from the first round with the ninth beam of SG-II laser facility, and the probe time is $T_0 + 3, 4, 5 \text{ ns}$ respectively. The location of CH target is labeled by the white box, and the position of Cu target is labeled by V-shape yellow box. We can clearly observe the evolution of Cu jet from collisionless to strong collision. For the panel (d) to (f) and panel (h), these experiment results are from the second round. In this round, the later evolution of the deflected jet is mainly concerned. Panel (d) is the shadowgraphy of CH background at $T_0 + 5 \text{ ns}$, and a very high density core is shown in front of CH target. The shadowgraphy and Nomarski images of $L_{\text{dist}} = 500\mu\text{m}$ at $T_0 + 5 \text{ ns}$ are given in panel (e) and (f) respectively. Panel (g) is the average pixel data along the vertical direction of the orange box in panel (a). The probe time of panel (h) is at $T_0 + 6 \text{ ns}$. And the color map of panel (i) is corresponding to the number density distribution in cm^{-3} of panel (f). The black dotted lines in panel (e), (f) and (h) are the position of the axis of Cu target.

The Cu plasma jet is accumulated in front CH hemisphere target and a double-shock structure is formed (as shown the red arrow in Fig. 4(c)). Then the jet is deflected downward along the direction of the first shock (4(d)). The other shock (the blue arrow in Fig. 4(c)) is close to the CH hemisphere target, and this target is nearly not compressed by this shock due to the high density.

The self-emitting X-rays from the interacting plasma is recorded by the pinhole camera (1(a)). The magnification is set to $\times 6$, and a $2 \mu\text{m}$ -thick aluminum (Al) foil filter is used, which can allow the X-rays energy above $\sim 400 \text{ eV}$ to pass. The related experimental results are shown in Fig. 4(f) to 4(i). The bulk plasma in the measurement region is considered as Maxwell-Boltzmann distribution, and the main radiation mechanism of X-rays is bremsstrahlung. The bremsstrahlung emission power per unit energy and volume is scaled as $J_{br}(\nu, T) \propto T^{-\frac{1}{2}} n_e n_i Z^2 e^{-h\nu/kT} (\text{erg s}^{-1} \text{cm}^{-3} \text{Hz}^{-1})$ ²⁹, where ν, T represent the photon frequency and temperature; and n_e, n_i, Z are the number density of electron, ion and the average ionic charge. We can integrate emission over the whole spectrum to get the power per volume scales as $T^{1/2} n_e n_i Z^2 (\text{erg s}^{-1} \text{cm}^{-3})$ ³⁰.

The images of self-emitting X-rays in Fig. 4 are obtained in the second experiment. And the results of first round are given in Supplementary Fig. S3, but its field of view is smaller. The X-ray self-emission of Cu plasma jet is shown in Fig. 4(f), and a collimation emission structure appears at the axis of V-shape Cu target. Its length is about $3000 \mu\text{m}$. For the case of $L_{\text{dist}} = 1500\mu\text{m}$, the main morphology of the emission is very similar to the result of 4(f), the plasma jet is minimally affected by the background. When the L_{dist} equals to $500 \mu\text{m}$ (4(h)), there is a $600 \mu\text{m}$ long luminous bright line under the CH target, and its position is close to the first shock (S_1 in 4(h)). The enhanced X-ray self-emission indicates that a strongly compressed and heated zone is formed in the interaction region. When the jet interacts with the CH hemisphere target, a double-layer emission structure is shown in 4(i), and this result is consistent with shadowgraph image at $T_0 + 6 \text{ ns}$ 4(c). This double-layer structure also proves that two stable shock zones are formed in front of CH hemisphere target. The emission characteristics is different with the case of $L_{\text{dist}} = 500\mu\text{m}$, and more detailed analysis is given in Discussion section.

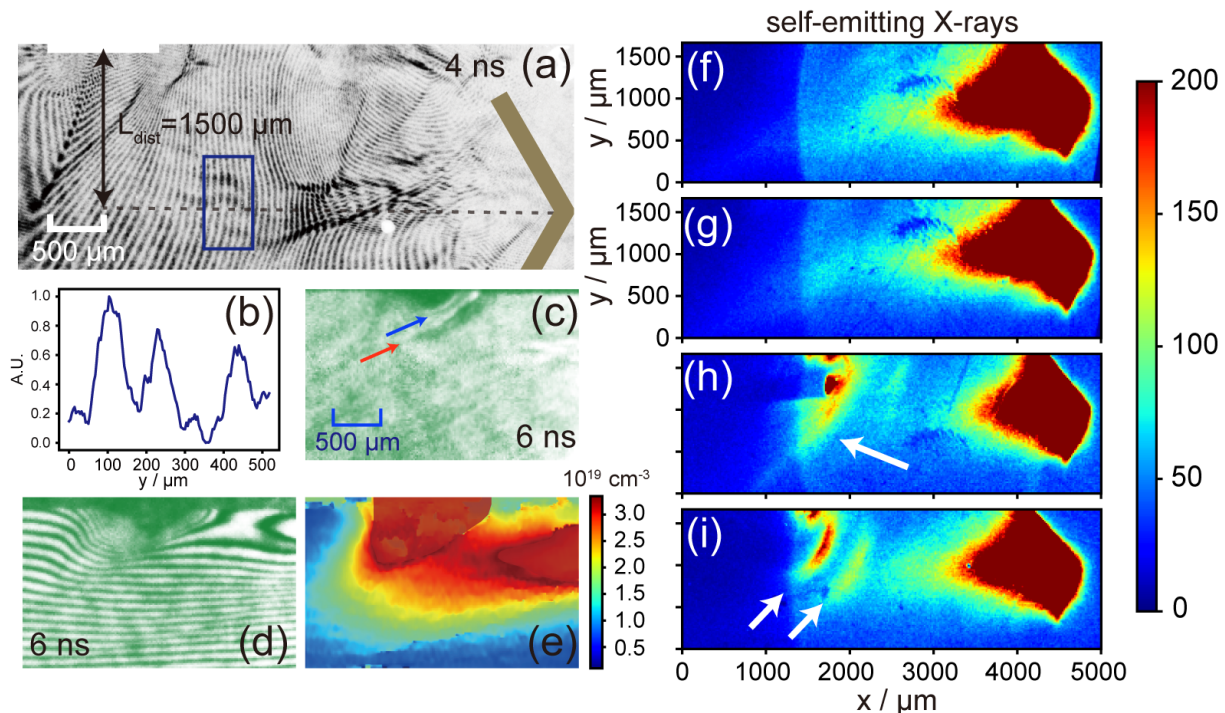


FIG. 4. **The optical images and the self-emitting X-rays through pinhole camera.** The panel (a) is corresponding to the case of $L_{\text{dist}} = 1500\mu\text{m}$ at the delay time is $T_0 + 4$ ns, and the interaction between jet and background is fully collisionless. Panel (b) is the average pixel data along the vertical direction of the blue box in panel (a). Panel (c) and (d) show the results of plasma jet directly interacts with the CH hemisphere target (1(g)) at $T_0 + 6$ ns, and panel (e) is corresponding to the number density distribution in cm^{-3} of panel (d). Panel (f) to (i) are the images of self-emitting X-rays through pinhole camera. Panel (f) is X-ray self-emission of Cu plasma jet, and panel (g) is the case of $L_{\text{dist}} = 1500\mu\text{m}$, which is fully collisionless. Panel (h) is the case of $L_{\text{dist}} = 500\mu\text{m}$, and panel (g) shows the case of CH hemisphere target.

According to the all experimental results mentioned above, the morphology and the radiation characteristics of the interaction between the jet and background are different in collision and collisionless situation. For the case of $L_{\text{dist}} = 500\mu\text{m}$ and hemisphere target, the strong collisions are dominated in the interaction zone, so we use the radiation magneto-hydrodynamics method to reproduce the experiment results. And more details are confirmed by the simulation results. For the fully collisionless situation, the particle-in-cell (PIC) method is applied here to simulate the process of plasma kinetic dynamics within background.

II. DISCUSSION

The PIC simulation for collisionless situation. In order to reproduce the experiment results in the collisionless case, we chose the typical data as the initial conditions of the PIC simulation. The Cu plasma jet is injected from the left boundary of simulation box, whose electron number density is $4 \times 10^{19} \text{ cm}^{-3}$ and the average ionization is $Z_{\text{Cu}} = 10$. The inject velocity is 1200 km/s, which equals the relative velocity observed within the experiment. The uniform CH background is set in the box. The electron number density of CH is $2 \times 10^{19} \text{ cm}^{-3}$, and the average ionization of CH is $Z_{\text{CH}} = 3.5$. The size of simulation box is $(L_x, L_y) = 2000 \mu\text{m} \times 2000 \mu\text{m}$, and the box is divided into $(N_x, N_y) = 500 \times 500$ grids, with 60 macro-particles per species are employed in each grid. The ion skin depth of CH is about $d_{i,\text{CH}} \approx 70 \mu\text{m}$, and the ratio of $d_{\text{CH},i}$ to the spatial resolution of simulation box is 17.5. The boundary conditions are open for both particles and fields.

To accelerate the PIC simulation, a self-similar transformation is applied in our simulation. More details are shown in Methods section. As shown in Fig 5, a Cu plasma jet is injected from the left boundary of the simulation box at 0 ns, and the ion number density of Cu plasma is shown in panel (a) and (b) at 0.6 ns and 0.9 ns respectively. The typical Weibel instability growth time is $\tau_w \approx c/(v_{\text{flow}}\omega_{pi}) = 0.056 \text{ ns}$. Within 0.6 ns, the instability produces filament-structure magnetic fields as 40 T (as shown in panel (c)), and the transverse wavelength of filaments is about $50\mu\text{m}$. At 0.9 ns, the transverse wavelength increase to about $80\mu\text{m}$ (as shown in Fig 5(f)), which is about ion skin

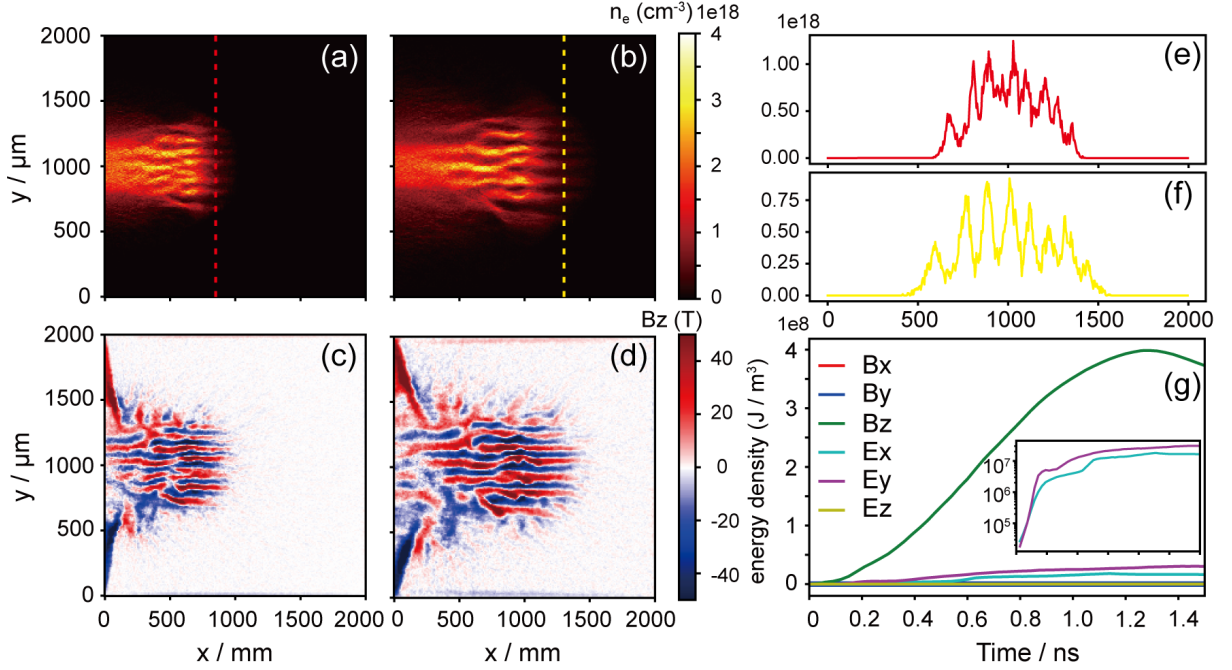


FIG. 5. **A PIC simulation for the collisionless case.** Cu plasma jet is injected from the left boundary of the box at 0 ns, and the uniform CH background is set in the box. The ion number density of Cu plasma is given in panel (a) and (b) at 0.6 ns and 0.9 ns respectively. The corresponding z-component magnetic fields (B_z) are plotted in panel (c) and (d). The number density distribution along the y direction at the front of Cu plasma jet is shown in (e) and (f). The red and yellow lines are corresponding to the red dot line in (a) and yellow dot line in (b). The box-averaged energy densities of the electric field (E_x, E_y, E_z) and magnetic field (B_x, B_y, B_z) are shown in panel (g), and the inside panel shows the energy densities of E_x and E_y .

depth.

The box-averaged energy densities³¹ of the electric field and magnetic field are calculated through $\epsilon_{E_i}(t) = (N_x N_y)^{-1} \sum_{i,j} \epsilon_0 [E_i(i\Delta_x, j\Delta_y, t)]^2 / 2$ and $\epsilon_{B_i}(t) = (N_x N_y)^{-1} \sum_{i,j} (B_i(i\Delta_x, j\Delta_y, t))^2 / (2\mu_0)$, where E_i, B_i represent different components of electric fields and magnetic fields; i, j are the grid number in x and y direction; Δ_x, Δ_y are the width of grid; ϵ_0, μ_0 are the vacuum permittivity and vacuum magnetic permeability respectively.

Fig 5(g) demonstrates that the box-averaged energy density of B_z increases exponentially firstly, and it is much larger than any other components. The energy density E_x and E_y are also amplified, and according to the inside figure of 5(g), the growth of the component E_x is a little smaller than E_y . The energy densities of the other field components nearly did not grow. The plasma kinetic energy converts to field energy and internal energy through Weibel instability and collective plasma effect, but the energy conversion efficiency is relatively low (only about 0.6% of kinetic energy).

The RMHD simulation for collision situation. To model the interaction between jets and background plasma, 3D numerical simulations are performed through the radiation magneto-hydrodynamics code FLASH³², and more details are given in Methods section. Figure 6(a) to (d) show the whole process of interaction between the Cu jet and CH background, and the distance L_{dist} is set as $500 \mu\text{m}$. The color maps correspond to the logarithmic mass density at different time. The total pressure is defined as $P_{\text{tot}} = P_{\text{thermal}} + P_{\text{ram}} = Nk_B T + \rho v^2$, where the two items on the right side represent the thermal pressure (P_{thermal}) and ram pressure (P_{ram}) respectively. And the total pressure of the Cu plasma jet and CH background at the axis of V-shape target, marked by the block dot line in 6(a) (from $x = 3 \text{ mm}$ to $x = 5 \text{ mm}$), is plotted in 6(i) to (l). The Cu and CH plasma can be distinguished through specie names in FLASH code. A shock detection method is also implemented in FLASH code, and more details can refer to the paper³³. The parameter of shock will be set to 1 if a strong shock structure is detected there, and Fig 6(s) plot the shock parameter at 5 ns.

At 2 ns, the low-density part of jet has reached the edge of CH background. And then, due to the higher total pressure of Cu plasma, the CH background is compressed. According to the shock parameter, a double-shock structure appears in the interaction region. The first shock is formed due to the collision of super-sonic plasma jet with the background. A mixed interaction region is formed (marked by white dot lines in Fig 6(d)), and the plasma jet is deflected downward along the direction of the first shock. The pressure of shocked CH plasma is higher than the

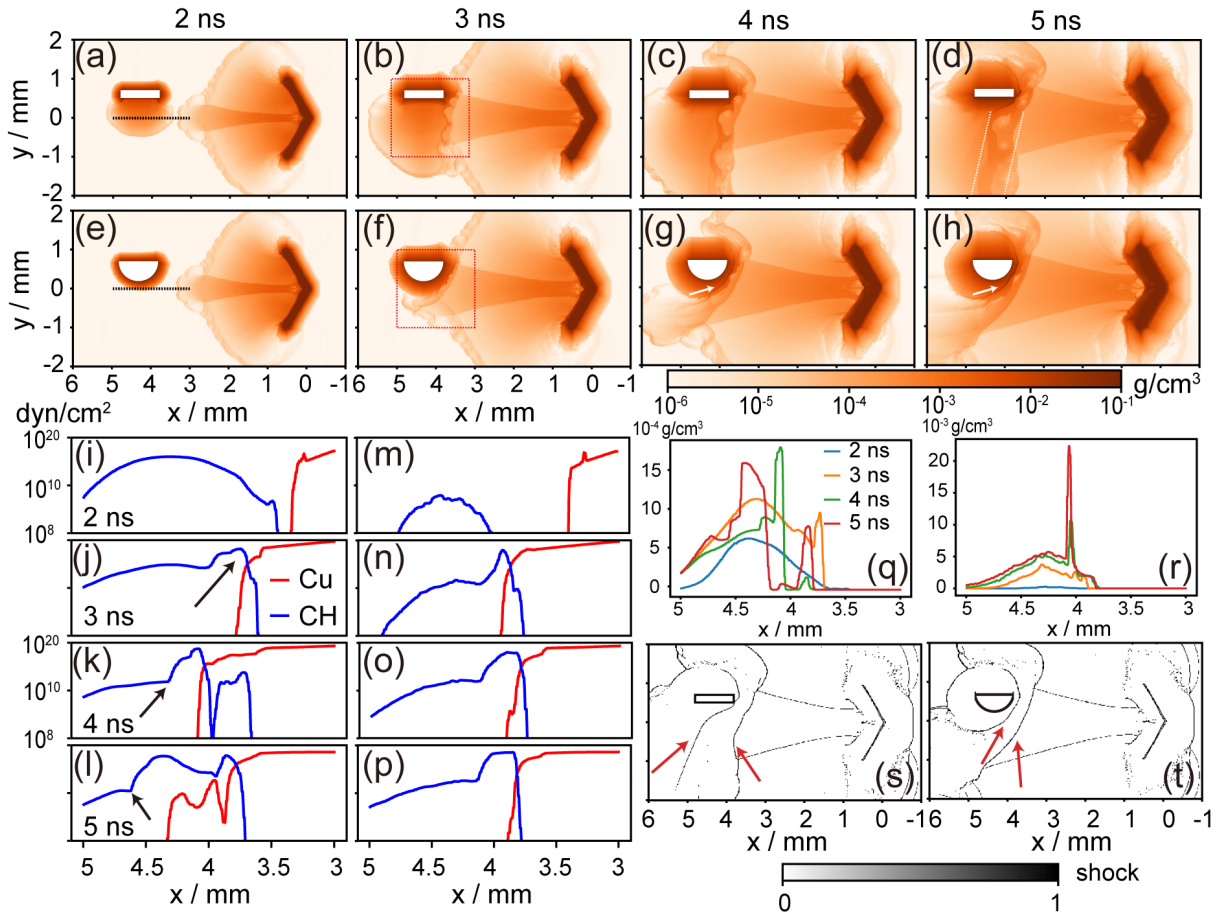


FIG. 6. **The simulation results for the strong collision case through radiation magneto-hydrodynamics code.** (a-h) The color maps correspond to the logarithmic density at different time, and the white blocks are the initial position of the CH target. Panel (a) to (d) show the interaction results of the case of $L_{\text{dist}} = 500\mu\text{m}$, and panel (e) to (h) represent the jet directly interacts with the CH hemisphere target. Panel (i) to panel (p) are the total pressure of the Cu plasma jet and CH background at the axis of V-shape target ($y = 0$) from $x = 3$ mm to $x = 5$ mm (labeled by the black dot line in (a) and (e)). Panel (i) to (l) correspond to the case of $L_{\text{dist}} = 500\mu\text{m}$, and panel (m) to (p) correspond to the other case. And the mass density of CH background at the same position is given in panel (q) and (r). Panel (s) and (t) plot the shock parameter of the two cases at 5 ns respectively.

undisturbed zone (as pointed by the black arrow in 6(j)). Then a forward shock moves inward to compress the CH background (as shown in 6(k) and (l)). The mass density of CH background is increased by 2 to 3 times compared with the undisturbed zone when the forward shock passes, as shown in 6(q). The peak mass density of CH also gradually moves inward, and the velocity is estimated as 250 km/s. Due to the post-shock jet and background plasma reach equilibrium, the speed of the shock in the background can be estimated^{12,17} as $v_{\text{back}} = (\rho_{\text{jet}}/\rho_{\text{back}})^{1/2}v_{\text{jet}}$, where $\rho_{\text{jet}}, \rho_{\text{back}}$ are the mass density of the Cu jet and background respectively. According to the simulation, the mass density ratio of the jet to the background is about 0.12, so the estimated speed is about 260 km/s, which is consistent with the experiments. The Kelvin-Helmholtz instability grows rapidly due to the difference of downward speed at the interface of CH and Cu. As shown in 7(a), the Biermann magnetic fields at the interface are amplified due to the compression of the plasma flow. The fields within the KH vortex are much higher than other places due to vortex motion of the plasma. This result shows that the self-generated magnetic fields is amplified through KH instability³⁴, and the charged particles may be accelerated by these amplified fields³⁵. And finally we have to point out, due to the single Eulerian fluid code, the plasma can not penetrate each other, so that the whole process of experiment, from collisionless to strong collision, cannot be fully reproduced by the radiation fluid simulation.

For the plasma jet directly interacts with the CH hemisphere target, the collision state is fully strong collision. The solid CH target is gradually ionized by the thermal radiation generated by the high temperature Cu plasma (6(e)). Similar to the former case, a strong shock is formed when the plasma jet interacts with the high-density background,

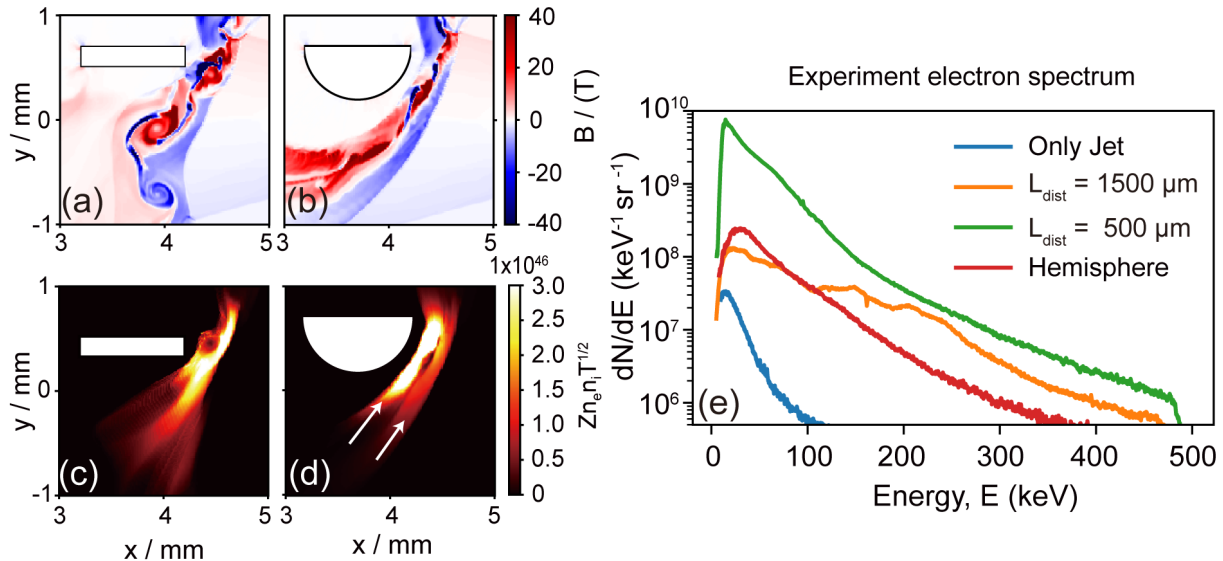


FIG. 7. **Integrated X-ray emission and self-generated magnetic at the interface and experimental electron spectrum.** The self-generated Biermann magnetic fields at the interface for both cases are also shown in panel (d) and (e), and their position are corresponded to the red boxes in 6(b) and (f) respectively. We integrate the $T^{1/2}n_e n_i Z^2$ at different moments to simulate the self-emitting X-ray data (c and d), and they can be compared with the experimental data. The white area represents the initial position of the target. The experimental time-integrated electron spectrum of different cases is given in panel (e).

but the Cu plasma jet can not move inward due to the higher pressure of CH plasma, as shown in 6(n) to (p). The Cu plasma jet is deflected downward at the first strong shock, and the deflection angle is about 50° , which is consistent with the experiment. A forward shock is also formed within the CH plasma, but its velocity is only about 30 km/s. A nearly quasi-static high-density structure is formed in front of the solid hemisphere target, as shown in by the white arrows in 6(h), which is similar to the experiments (4(c)) and also in line with theoretical predictions. The mass density of CH plasma is one order of magnitude higher than the former case. And the critical unstable mode of KH instability is $[g(\rho_2^2 - \rho_1^2)]/[\rho_1 \rho_2 (U_2 - U_1)^2]$, then the large-wave KH instability is suppressed due to the much higher density background. The results of self-generated fields also show that there is no large-scale KH vortex.

After the shock wave passes, the temperature of the shocked region will rise rapidly, and the self-emitting X-rays of plasma will also increase accordingly. As we analyzed above, the the power per volume of self-emitting X-rays scales as $T^{1/2}n_e n_i Z^2$ ($erg s^{-1} cm^{-3}$), so we can integrate the corresponding data at different moments to get the total emitting image. And the detail of the integration method is given in Method section. Fig 7(a) and (b) plot the integration data. For the case of $L_{dist} = 500 \mu m$, a strong emission layer is formed in front of the CH plain target, and this is also the location of the first shock wave. The integrated emission of the forward shock within the CH background is not strong due to the compression velocity is very high. While for the CH hemisphere case, a double-layer emission structure is formed, and the intensity of the inner layer is much higher. And this structure is homologous with the two stable shocks in 6(t). The strong inner emission layer is because of the quasi-static forward shock within CH plasma. And both of the emission characters are consistent with the experiment results (4(h) and (i)).

Comparing with the measured time-integrated electron spectrum in jet-only case (blue line in 7(e)) and the interaction case, we can find some significant differences between them. When the only plasma jet is produced, the measured electron spectrum shows that a much lower number ($< 20.6\%$) and energy ($< 16\%$) of electrons above 40 keV. And there is almost no signal for the background-only case. While for the interaction cases, the thermal temperature (the peak position) of electrons is higher, and the electrons can be accelerated up to higher energy. Therefore, our electron spectrometer measurements indicate that some acceleration mechanisms are present for the interaction. According to the previous experiments and simulations^{36–38}, the charged particles can be accelerated by the Weibel-dominated electromagnetic shock in the collisionless plasma. There are also filament structures in our experiment results. And the electrons may be accelerated by the electromagnetic structures induced by the Weibel instability. We have to point out that the collisionless shock is not formed in our experiments. For collision cases, the electrons can be accelerated by the vortex-like magnetic field cloud structures induced by the KH instability through Fermi acceleration mechanism³⁹. The cut-off energy and quantity of hemisphere obstacle case is lower than

the $L_{dist} = 500 \mu m$ case may be due to the KH instability is suppressed in the former case. All the above inferences are based on our experimental data and simulation results, and we will continue to analyse acceleration mechanisms in the future.

Applied to the HH objects. According to the scaling laws, if the laboratory experiments scale up to the astrophysical objects, both plasma flows should share similar dimensionless parameters. Similar to the HH objects, the Reynolds number (R_e) and Peclet number (P_e) are much larger than unity. And the Mach number of jet is also larger than unity. For the collision case ($L_{dist} = 500 \mu m$), the collisionality parameter $\zeta = \lambda_{mfp}/L_{system}$ at the core part is greater than unity, which satisfies the localization criteria. Then the scaling laws confirm that similarity between the HH 110/270 system and the laboratory experiments under the following transformation, $r_{ast} = ar_{lab}, \rho_{ast} = b\rho_{lab}, p_{ast} = cp_{lab}, t_{ast} = a\sqrt{b/ct_{lab}}, v_{ast} = \sqrt{c/b}v_{lab}$, where a, b, c are the transformation parameters, r, ρ, p, t, v represent characteristic length, mass density, pressure, time and velocity respectively. The subscript ast represent the astrophysical objects, and lab represents the laboratory experiments. The transformation coefficients are calculated as $a = 3.3 \times 10^{15}, b = 5.4 \times 10^{-17}, c = 3.2 \times 10^{-18}$ with the relevant parameters, and more details are given in Supplementary. The scaled parameters of the laser-driven plasma are very similar to the HH 110/270 system, and the similarity criteria also confirm that our results can be applied to the astrophysical scale. Our results indicate that the KH instability at the interface may lead to the complex and chaotic structure of HH 110 jet. The impact point would be compressed into the inside part of the dense cloud due to the forward shock, and this experiment result verifies the Raga's inference (The impact point of HH 270 has moved deeper into the cloud, at the westward of the HH 110 axis.)¹⁸. These results can explain the substantial HCO⁺ emission¹³ at the west of the HH 110 is produced by the forward shock within the cloud. If the cloud is dense enough, the impact point would be close to the contact interface, and another substantial emission would appear, just like the hemisphere case in our experiment.

Our results provide the detailed interaction process between plasma jet and background plasma under different collision state. These findings can be applied to explain the relevant shock phenomena of the HH deflection system. And this experiment platform can also be adapted to other shock configurations, such as the collisionless shocks with counter-streaming plasma jets. This controlled laboratory laser-driven platform can greatly complement astrophysical observations, and also be used to validate the deflection model of HH objects.

III. METHODS

Experimental setup. The experiments were conducted at the at ShenGuang-II (SG-II) laser facility in Shanghai, China. The background plasma is generated by the laser-driven CH plain target or the hemisphere target. The plasma jet is produced by a V-shaped Cu target, which is constructed with two $500 \mu m$ thick Cu foils. And each foil is driven by two laser beams. Each driven laser (wavelength $\lambda_L = 351 \text{ nm}$) are smoothed through the continuous phase plate (CPP) with 250 J in 1 ns, and the diameter of each focal spot is about $600 \mu m$, resulting in the average intensity of $2.5 \times 10^{13} \text{ W/cm}^2$. The main diagnostics are optical probe a 527 nm probe beam, pinhole X-ray camera and electron spectrometer. A $2 \mu m$ -thick aluminum (Al) foil filter is used in the pinhole camera, and the electron spectra recorded in the electron spectrometer range from 20 to 500 keV. The intensity of the uniform magnetic field was set as 600 G, which was generated by two permanent magnets, more details can refer the paper⁴⁰.

Collision parameter For the collisions between the species α, β of the counter-streaming flows, the mean free path can be expressed as $\lambda_{\alpha\beta} = m_{\alpha\beta}^2 v_r^4 \ln \Lambda_{\alpha\beta} / (4\pi Z_\alpha^2 Z_\beta^2 e^4 n_\beta)$ ^{38,41}, where $m_{\alpha\beta}, v_r, Z_\alpha \text{ or } \beta, \ln \Lambda_{\alpha\beta}$, and n_β respectively represent the reduced mass, relative velocity, average ionization state, the Coulomb logarithm and the mean number density. And the reduced mass can be calculated as $m_{\alpha\beta} = m_\alpha m_\beta / (m_\alpha + m_\beta) = A_\alpha A_\beta / (A_\alpha + A_\beta)$, where $A_\alpha \text{ or } \beta$ is the atomic mass number for different species. According to the simulation and experiment results, these parameters for Cu and CH plasma can be estimated as $v_r = 1.2 \text{ km/s}, A_\alpha = 64, A_\beta = 6.5, \bar{Z}_\alpha \approx 10, \bar{Z}_\beta \approx 3.5, \ln \Lambda_{\alpha\beta} \approx 8$, then the mean free path can be calculated through the formula above.

The integration method of self-emitting X-rays Due to the $2 \mu m$ -thick aluminum (Al) foil filter in the pinhole camera, only the X-rays energy above $\sim 400 \text{ eV}$ can be recorded. And according to the Bethe-Heitler formula⁴², the differential cross-section $Q_\varepsilon(E)$ (where E is the electron energy) of photon energy ε is $Q_\varepsilon(E) = \frac{8}{3} \frac{r_0^2}{137} \frac{mc^2}{\varepsilon E} \log \frac{1+\sqrt{1-\varepsilon/E}}{1-\sqrt{1-\varepsilon/E}}$, where m and r_0 are the rest mass and classical radius of the electron, and c is the light speed. Therefore, photons with 400 eV energy are mainly emitted by electrons with a temperature higher than 800 eV, so we select the area where the temperature is greater than 800 eV to integrate. The the power per volume of self-emitting X-rays scales as $T^{1/2} n_e n_i Z^2 \text{ (erg s}^{-1} \text{ cm}^{-3}\text{)}$, so that the corresponding data at different moments is integrated to get the total emitting images in the simulations.

Numerical simulations The radiation-magneto-hydrodynamics code FLASH³² is used to model the laser absorption and the plasma interaction of strong collision case. The target configuration and the laser parameters, such as incident angles, focal size and pulse duration are accordance with the experiments. For the simulation free expansion

of CH plasma, a $x \times y \times z = 3 \text{ mm} \times 3 \text{ mm} \times 4 \text{ mm}$ simulation box is set. The adaptive mesh refinement method is applied in the simulations, and the maximum resolution is $10 \mu\text{m}$. A laser beam is incident on the target surface obliquely. For the simulation of jet-only case, the computational domain is set as $x \times y \times z = 7 \text{ mm} \times 4 \text{ mm} \times 4 \text{ mm}$ with the maximum resolution $10 \mu\text{m}$. For the plasma interaction cases, two-dimensional simulation is performed to achieve higher resolution accuracy. The computational domain of 2D simulation is set as $x \times y = 7 \text{ mm} \times 4 \text{ mm}$, and the maximum resolution is about $4 \mu\text{m}$. The self-generated Biermann magnetic field is also include in our simulations.

PIC simulation For the collisionless case, two-dimensional PIC simulation of plasma interaction are performed with the fully electromagnetic and massively parallel PIC code Epoch 4.17⁴³. In order to better reproduce the experimental results, a self-consistent transform method is applied in our simulation. Similar to the scaling laws of the magneto-hydrodynamic equations, a set of parameters to transform the plasma states of experiment data to adapt to the PIC simulation, and the key dimensionless number (such as plasma β , Mach number, etc) of both systems keep conserved⁴⁴. Coulomb collisions are well included by keeping L_{system}/λ_{ii} preserved, and the L_{system}/d_i where $d_i = c/\omega_{pi} = c/(4\pi n_i Z^2 e^2/m_i)^{1/2}$ also remains unchanged to ensure the two-fluid effect keeps same in both systems. The details of the self-similar transformation are given as follows.

$$L_{PIC} = f_L L_{exp}, m_{i,PIC} = f_m m_{i,exp}, n_{i,PIC} = f_n n_{i,exp}, T_{PIC} = f_T T_{exp}$$

$$t_{PIC} = f_L \sqrt{f_m/f_T} t_{exp}, v_{PIC} = \sqrt{f_T/f_m} v_{exp}, B_{PIC} = \sqrt{f_n f_T} B_{exp}$$

where L, m, n, T represent the size, ion mass number, number density and temperature respectively; the t, v, B represent time, velocity and magnetic field strength. Here we choose the $f_n = 1$ to keep the number density unchanged in two systems, and $f_m = 0.05$ to reduce the ion mass number in PIC simulation. To remain L_{system}/d_i unchanged, we can obtain that $f_r = \sqrt{f_m/f_n}$. $f_T = 5$ is set in our simulation. According to these transformation parameters, the PIC simulation can be accelerated.

DATA AVAILABILITY

The data that support the findings of this study are available from the corresponding authors upon reasonable request.

CODE AVAILABILITY

FLASH is an open adaptive mesh refinement hydromagnetic code, which is developed by the Flash Center for Computational Science at the University of Chicago. The open source code is available for requested from <http://flash.uchicago.edu/site/flashcode/coderequest/>.

EPOCH is an open source PIC code for high energy density physics, which is fully electromagnetic and massively parallel. It is developed by the university of Warwick, and the code is available from <https://github.com/Warwick-Plasma/epoch/releases>.

IV. REFERENCES

- ¹Reipurth, Bo, and John Bally. "Herbig-Haro flows: Probes of early stellar evolution." *Annual Review of Astronomy and Astrophysics* 39.1 (2001): 403-455.
- ²Bally, John. "Protostellar outflows." *Annual Review of Astronomy and Astrophysics* 54 (2016): 491-528.
- ³Mirabel, I. F., et al. "Jet-induced star formation by a microquasar." *Proceedings of the International Astronomical Union* 10.S313 (2014): 370-373.
- ⁴Fragile, P. Chris, et al. "Numerical Simulations of a Jet-Cloud Collision and Starburst: Application to Minkowski's Object." *The Astrophysical Journal* 850.2 (2017): 171.
- ⁵Man, Allison WS, et al. "Quenching by gas compression and consumption-A case study of a massive radio galaxy at $z = 2.57$." *Astronomy and Astrophysics* 624 (2019): A81.
- ⁶Gilli, Roberto, et al. "Discovery of a galaxy overdensity around a powerful, heavily obscured FR II radio galaxy at $z = 1.7$: star formation promoted by large-scale AGN feedback?." *Astronomy and Astrophysics* 632 (2019): A26.
- ⁷Mukherjee, Dipanjan, et al. "Relativistic jet feedback-III. Feedback on gas discs." *Monthly Notices of the Royal Astronomical Society* 479.4 (2018): 5544-5566.
- ⁸Gaibler, Volker, et al. "Jet-induced star formation in gas-rich galaxies." *Monthly Notices of the Royal Astronomical Society* 425.1 (2012): 438-449.

- ⁹Blandford, Roger, and David Eichler. "Particle acceleration at astrophysical shocks: A theory of cosmic ray origin." *Physics Reports* 154.1 (1987): 1-75.
- ¹⁰Koyama, K., Petre, R., Gotthelf, E. et al. Evidence for shock acceleration of high-energy electrons in the supernova remnant SN1006. *Nature* 378, 255–258 (1995).
- ¹¹Aharonian, F., Akhperjanian, A., Aye, KM. et al. High-energy particle acceleration in the shell of a supernova remnant. *Nature* 432, 75–77 (2004).
- ¹²Reipurth, B., A. C. Raga, and S. Heathcote. "HH 110: the grazing collision of a Herbig-Haro flow with a molecular cloud core." *Astronomy and Astrophysics* 311 (1996): 989-996.
- ¹³Choi, Minho. "Observations of Molecular Clouds in the HH 270/110 Region." *The Astrophysical Journal* 550.2 (2001): 817.
- ¹⁴Kajdic, P., et al. "Proper motions of the HH 110/270 system." *The Astronomical Journal* 143.5 (2012): 106.
- ¹⁵Riera, A., et al. "Fabry-Pérot observations of the HH 110 jet." *The Astronomical Journal* 126.1 (2003): 327.
- ¹⁶De Young, David S. "The deflection of cosmic jets." *The Astrophysical Journal* 371 (1991): 69-81.
- ¹⁷Raga, A. C., and J. Cantó. "The initial stages of an HH jet/cloud core collision." *Revista Mexicana de Astronomía y Astrofísica* 31 (1995): 51-61.
- ¹⁸Raga, A. C., et al. "Jet/cloud collision, 3D gasdynamic simulations of HH 110." *Astronomy & Astrophysics* 392.1 (2002): 267-276.
- ¹⁹Remington, B. A. Modeling Astrophysical Phenomena in the Laboratory with Intense Lasers. *Science* 284, 1488–1493 (1999).
- ²⁰Remington, B. A., Drake, R. P. & Ryutov, D. D. Experimental astrophysics with high power lasers and Z pinches. *Rev. Mod. Phys.* 78, 755–807 (2006).
- ²¹Lebedev, S. V., Frank, A. & Ryutov, D. D. Exploring astrophysics-relevant magnetohydrodynamics with pulsed-power laboratory facilities. *Rev. Mod. Phys.* 91, 025002 (2019).
- ²²Ryutov, D., et al. "Similarity criteria for the laboratory simulation of supernova hydrodynamics." *The Astrophysical Journal* 518.2 (1999): 821.
- ²³Ryutov, D. D., et al. "Magnetohydrodynamic scaling: From astrophysics to the laboratory." *Physics of Plasmas* 8.5 (2001): 1804-1816.
- ²⁴Lebedev, S. V., et al. "Jet deflection via crosswinds: Laboratory astrophysical studies." *The Astrophysical Journal* 616.2 (2004): 988.
- ²⁵Yuan, Dawei, et al. "Modeling Supersonic-Jet Deflection in the Herbig–Haro 110-270 System with High-Power Lasers." *The Astrophysical Journal* 815.1 (2015): 46.
- ²⁶Hartigan, P., et al. "Laboratory experiments, numerical simulations, and astronomical observations of deflected supersonic jets: Application to HH 110." *The Astrophysical Journal* 705.1 (2009): 1073.
- ²⁷Li, C. K., et al. "Structure and dynamics of colliding plasma jets." *Physical review letters* 111.23 (2013): 235003.
- ²⁸Ryutov, D. D., et al. "Collisional effects in the ion Weibel instability for two counter-propagating plasma streams." *Physics of Plasmas* 21.3 (2014): 032701.
- ²⁹Halverson, W. "Bremsstrahlung photon emission rate from Maxwellian plasmas." *Plasma Physics* 14.6 (1972): 601.
- ³⁰Rybicki, George B., and Alan P. Lightman. *Radiative processes in astrophysics*. John Wiley & Sons, 1991.
- ³¹Stockem A, Dieckmann M E, Schlickeiser R. PIC simulations of the thermal anisotropy-driven Weibel instability: field growth and phase space evolution upon saturation[J]. *Plasma Physics and Controlled Fusion*, 2009, 51(7): 075014.
- ³²Fryxell, Bruce, et al. "FLASH: An adaptive mesh hydrodynamics code for modeling astrophysical thermonuclear flashes." *The Astrophysical Journal Supplement Series* 131.1 (2000): 273.
- ³³Balsara, Dinshaw S., and Daniel S. Spicer. "A staggered mesh algorithm using high order Godunov fluxes to ensure solenoidal magnetic fields in magnetohydrodynamic simulations." *Journal of Computational Physics* 149.2 (1999): 270-292.
- ³⁴Alves, E. P., et al. "Large-scale magnetic field generation via the kinetic Kelvin-Helmholtz instability in unmagnetized scenarios." *The Astrophysical Journal Letters* 746.2 (2012): L14.
- ³⁵Borse, Nikhil, et al. "Numerical study of the Kelvin-Helmholtz instability and its effect on synthetic emission from magnetized jets." *Astronomy & Astrophysics* 649 (2021): A150.
- ³⁶Huntington, C. M., et al. "Observation of magnetic field generation via the Weibel instability in interpenetrating plasma flows." *Nature Physics* 11.2 (2015): 173-176.
- ³⁷Li, C. K., et al. "Collisionless shocks driven by supersonic plasma flows with self-generated magnetic fields." *Physical review letters* 123.5 (2019): 055002.
- ³⁸Fiuza, F., et al. "Electron acceleration in laboratory-produced turbulent collisionless shocks." *Nature physics* 16.9 (2020): 916-920.
- ³⁹Zhang, Weiqun, Andrew MacFadyen, and Peng Wang. "Three-dimensional relativistic magnetohydrodynamic simulations of the kelvin-helmholtz instability: Magnetic field amplification by a turbulent dynamo." *The Astrophysical Journal Letters* 692.1 (2009): L40.
- ⁴⁰Liu, Huiya, et al. "Design and calibration of hot-electron spectrometer array for angle-resolved measurement." *Review of Scientific Instruments* 88.5 (2017): 053507.
- ⁴¹Chenais-Popovics, C., et al. "Kinetic to thermal energy transfer and interpenetration in the collision of laser-produced plasmas." *Physics of Plasmas* 4.1 (1997): 190-208.
- ⁴²Brown, John C. "The deduction of energy spectra of non-thermal electrons in flares from the observed dynamic spectra of hard X-ray bursts." *Solar Physics* 18.3 (1971): 489-502.
- ⁴³Arber, T. D., et al. "Contemporary particle-in-cell approach to laser-plasma modelling." *Plasma Physics and Controlled Fusion* 57.11 (2015): 113001.
- ⁴⁴Zhao Z.H., et al. "Laboratory observation of plasmoid-dominated magnetic reconnection in hybrid collisional-collisionless regime." Submitted to *Nature physics*.

ACKNOWLEDGEMENTS

The authors thank the staff of the ShenGuang (SG) – II laser facility for operating the laser system. This work is supported by the Science Challenging Project, No. TZ2018005, the NSAF, Grant No. U1630246; the National Key Program of S&T Research and Development, Grant No. 2016YFA0401100; the National Natural Science Foundation of China, Grants No. 11575298 and 11825502. BQ acknowledges Supported from National Natural Science Funds for

Distinguished Young Scholar, Grant No. 11825502. The simulations are carried out on the Tianhe-2 supercomputer at the National Supercomputer Center in Guangzhou.

AUTHOR CONTRIBUTIONS

All authors contributed to the discussions and approved the final version of the manuscript.

COMPETING INTERESTS

The authors declare no competing interests.

ADDITIONAL INFORMATION

Correspondence and requests for materials should be addressed to B.Qiao.